




New synthesis route of highly porous $\text{In}_x\text{Co}_4\text{Sb}_{12}$ with strongly reduced thermal conductivity

N. Gostkowska-Lekner^{1,2,3}, B. Trawinski¹, A. Kosonowski^{4,5,*} , B. Bochentyn¹, M. Lapinski¹, T. Miruszewski¹, K. Wojciechowski^{4,5}, and B. Kusz¹

¹Department of Solid State Physics, Faculty of Applied Physics and Mathematics, The Gdansk University of Technology, ul. G. Narutowicza 11/12, 80-233 Gdańsk, Poland

²Helmholtz-Zentrum Berlin für Materialien und Energie, Hahn-Meitner Platz 1, 14109 Berlin, Germany

³Institut für Physik und Astronomie, Universität Potsdam, Karl-Liebknecht-Straße 24-25, 14476 Potsdam, Germany

⁴Department of Inorganic Chemistry, Faculty of Materials Science and Ceramics, AGH University of Science and Technology, Al. Mickiewicza 30, 30-059 Kraków, Poland

⁵The Lukasiewicz Research Network - Cracow Institute of Technology, Zakopianska 73, 30-418 Krakow, Poland

Received: 25 March 2020

Accepted: 9 June 2020

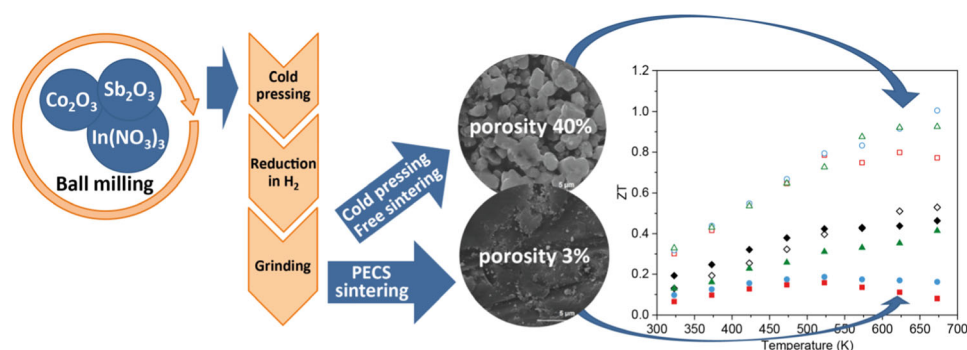
© The Author(s) 2020

ABSTRACT

Highly porous, In-filled CoSb_3 skutterudite materials with an attractive thermoelectric figure of merit ($ZT \sim 1$) and corresponding dense samples were fabricated through the cost-effective method of reduction in oxides in dry hydrogen and the pulsed electric current sintering (PECS) method, respectively. The reduction process was described in detail using in situ thermogravimetric analysis of Co_2O_3 , Sb_2O_3 and $\text{In}(\text{NO}_3)_3 \cdot 5\text{H}_2\text{O}$ separately and in a mixture. Two methods to synthesise the same material were examined: (a) free sintering of an initially reduced powder and (b) PECS. The free-sintered materials with higher porosities (up to $\sim 40\%$) exhibited lower values of electrical conductivity than the dense PECS samples (porosity up to $\sim 5\%$), but the benefit of an even sixfold reduction in thermal conductivity resulted in higher ZT values. The theoretical values of thermal conductivity for various effective media models considering randomly oriented spheroid pores are in good agreement with the experimental thermal conductivity data. The assumed distribution and shape of the pores correlated well with the scanning electron microscope analysis of the microstructure. The lowest value of thermal conductivity, equal to 0.5 W/m K , was measured at 523 K for $\text{In}_{0.1}\text{Co}_4\text{Sb}_{12}$ with 41% porosity. The highest value of $ZT_{\text{max}} = 1.0$ at 673 K was found for the $\text{In}_{0.2}\text{Co}_4\text{Sb}_{12}$ sample in which the porosity was 36% .

Address correspondence to E-mail: arturk@agh.edu.pl

GRAPHIC ABSTRACT



Introduction

Thermoelectric (TE) materials are being widely investigated and developed due to their potential applications for the construction of devices that allow direct conversion of heat into electrical energy. The advantages of these devices, i.e. small weight and size, simple construction and high reliability, are attractive for the construction of devices improving the efficiency of, for example, automotive drivetrains, power plants and other energetic devices for the recovery of waste heat. The main barriers to this technology are their still inadequate efficiency and quite high costs of production. However, continuous progress in thermoelectric materials engineering results in the improvement in energy conversion efficiency and the reduction in production costs.

The thermoelectric performance of a thermoelectric material is characterised by the so-called dimensionless figure of merit, $ZT = T(S^2\sigma)/\kappa_{\text{tot}}$, where S is the Seebeck coefficient, σ is the electrical conductivity and κ_{tot} is the total thermal conductivity, which consists of two components: the lattice thermal conductivity κ_l and the electrical thermal conductivity κ_e . Therefore, to obtain satisfactory performance of TE materials, it is necessary to enhance their thermoelectric properties, such as their Seebeck coefficient and electrical conductivity, and to decrease their total thermal conductivity.

Among various thermoelectric materials, skutterudites, particularly those based on cobalt

triantimonide CoSb_3 , have attracted the attention of researchers [1–5] mainly due to their excellent electronic properties and the relatively low price of their constituent elements. Skutterudites crystallise in the $Im\bar{3}$ body-centred cubic structure. The structure, presented in Fig. 1, consists of Sb atoms in the 24 g (0, x , y) Wyckoff position. The strongest Sb–Sb bonds form rectangles with shorter bonds (2.92 Å, all given bond lengths are obtained from a Rietveld refinement

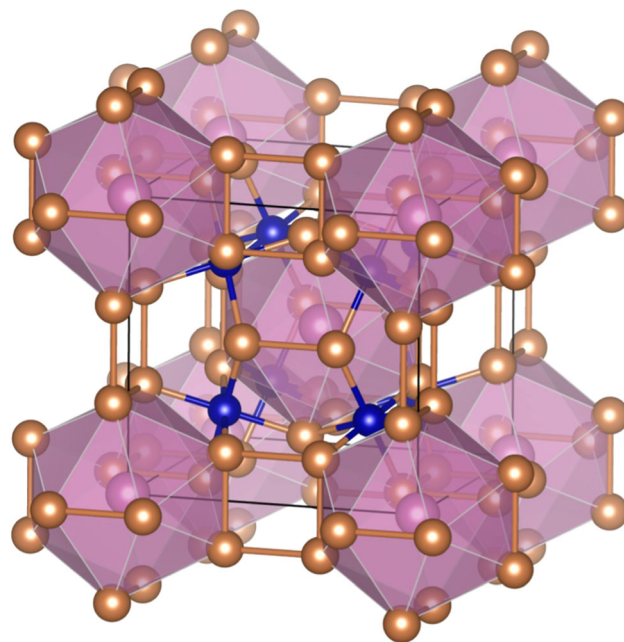


Figure 1 Crystal structure of In-filled CoSb_3 . Orange atoms—Sb, blue—Co, purple—In. For clarity, the figure presents fully filled skutterudite, corresponding to the $\text{InCo}_4\text{Sb}_{12}$ composition.

of the PECS01 sample investigated in this paper) forming polyhedra marked in purple, and longer ones (2.97 Å) between the polyhedra. The other Sb–Sb bonds on the polyhedra are weaker (3.71 Å). The antimony rectangles are joined by Co atoms in position 8c (0.25, 0.25, 0.25) with 2.52 Å bonds. The unit cell contains two cages (polyhedra marked in purple in Fig. 1), centred in the 2a (0, 0, 0) position that are large enough to accommodate a metal atom and create a so-called filled skutterudite ($\text{RCo}_4\text{Sb}_{12}$) [6]. The filling atom, R, is weakly bound to the antimony atoms. The length of the bonds is 3.36 Å, which is more than the sum of the corresponding atomic radii of 3.00 Å (in the case of In filling). Thus, the filling atom may act as a “rattler”, which can enhance phonon scattering and thus lower the thermal conductivity. Additionally, the filling atom acts as electron donor, improving the electrical conductivity. The lower values of thermal conductivity and higher electrical conductivity of filled skutterudites are in agreement with the phonon glass–electron crystal (PGEC) concept [7]. Many dopants are considered to be promising candidates, i.e. alkaline metals (Na [8], Li [9], Ba [10]), rare-earth metals (e.g. Yb $ZT_{\text{max}} = 1.4$ at 823 K [11], Ce $ZT_{\text{max}} = 1.3$ at 850 K [1]) and In ($ZT_{\text{max}} = 1.5$ at 725 K) [12]. The intermediate temperature range (670–870 °C) at which the skutterudites’ ZT parameter is the highest makes these materials excellent candidates for many applications, for example in the automotive industry [13, 14]. Skutterudites are relatively cheap in comparison with other materials currently used in thermoelectric modules. For example, the estimated cost of production of 1 kg of raw material in the case of Si–Ge alloy is USD 679; for Bi_2Te_3 , it is USD 110; and for skutterudites, it is USD 10–37 [15–17]. However, large-scale and low-cost production technologies have not been developed yet for these materials.

Typical powder metallurgy methods, commonly used in laboratories for the synthesis of skutterudites, often require pure metals as raw elements and a long synthesis procedure lasting up to 7 days and consisting of several stages, such as annealing, grinding and consolidation [18, 19]. Moreover, because of the high volatility of Sb, sealed quartz ampules are usually applied, which influences the costs of synthesis [18–21]. Therefore, for large-scale production of TE materials, faster and cheaper production methods need to be developed. Several rapid fabrication techniques have been proposed for the Co–Sb system.

Melt-spinning [22], microwave synthesis [23] and melting and quenching in air [12] have been successfully used to produce CoSb_3 -based skutterudites.

The reduction in reagents in the form of metal oxides in a hydrogen atmosphere may be an alternative route to large-scale production of TE materials. This method may be cheaper because of the lower price of oxides in relation to high purity metals, and due to the shorter synthesis time. Furthermore, it does not require any specialised and expensive equipment. And finally, most importantly, it is possible to obtain a relatively large porosity, which may be favourable for the further reduction in costs and increase in the materials’ ZT. The reduction in oxides with gaseous agents generally takes place at the surface of the oxide grains where surface defects have been found to play an important role in the reaction [24, 25]. Therefore, milling of the reduced powder prior to the reduction process enhances the rate of this process and allows it to be performed at a lower temperature. Additionally, in some mixtures of oxides, these oxides or reduced metals can have a catalytic effect on the process [26].

Synthesis of porous thermoelectric materials such as Bi_2Te_3 [27–29], $(\text{Bi,Sb})_2\text{Te}_3$ [29–31], $\text{Ge}_{0.77}\text{Ag}_{0.1}\text{Sb}_{0.13}\text{Te}$ (TAGS) [32], $\text{Bi}_2\text{Te}_{1-x}\text{Se}_x$ [33, 34] and CsBi_4Te_6 [35] via this technique has been previously reported. In this method, a mixture of oxides is reduced at a given temperature in a dry hydrogen flow. Controlling the temperature and time of the reduction, as well as the initial stoichiometry, leads to different final compositions, grain sizes, porosities and the overall thermoelectric properties of the material. Reduction in hydrogen was also used as part of a CoSb_3 chemical alloying fabrication process by Khan et al. [36] and chemical co-precipitation by Kim et al. [37]; however, the porosities of the obtained materials were relatively low (< 10%). Other thermoelectric materials with slightly higher porosity (~ 14%) were recently reported [38, 39], and in both cases, significant enhancement of the ZT parameter was observed due to the presence of pores.

The idea of a bulk skutterudite material with high (e.g. $\phi = 30\text{--}40\%$) porosity, which maintains high TE performance, is in our opinion worthy of further exploration. Therefore, in this study, the PECS and a cost-effective method of reduction in oxide reagents in hydrogen were used to fabricate highly porous, In-filled CoSb_3 skutterudite $\text{In}_x\text{Co}_4\text{Sb}_{12}$ ($x = 0.1, 0.2, 0.4$,

1). The microstructural and structural properties of the materials were analysed and compared with dense samples prepared by pulsed electric current sintering (PECS). Detailed analyses of the impact of the porosity (e.g. the shape and orientation of the pores) on the thermal and electrical transport properties, as well as the thermoelectric performance of the materials, were performed.

Experimental

The $\text{In}_x\text{Co}_4\text{Sb}_{12}$ ($x = 0.1, 0.2, 0.4, 1$) materials were prepared by the reduction in metal oxides in dry hydrogen. A stoichiometric mixture of Co_2O_3 (99%), Sb_2O_3 (Sigma Aldrich, 99.99%) and $\text{In}(\text{NO}_3)_3 \cdot 5\text{H}_2\text{O}$ (Sigma Aldrich, 99.9%) was ball-milled for 22 h at a rate of 350 rpm in a zirconia vessel with zirconia balls (diameter 3 mm). The ingredients were mixed with isopropanol with a ball-to-powder-weight ratio of 3:1. Then, the mixed starting reactants were cold-pressed at a uniaxial pressure of 6 MPa and reduced in an atmosphere of flowing H_2 at 600 °C for 2 h. It should be noted that in the case of $\text{In}(\text{NO}_3)_3 \cdot 5\text{H}_2\text{O}$ as a reactant, the step preceding the actual reduction process in hydrogen is the prior dehydration and decomposition of nitrate. After preliminary reduction, the materials were ground in an agate mortar, and 1.3 ml of 2% polyvinyl alcohol (PVA) in a water solution per 1 g of the powder was added as a binder and pore-forming agent. The powders were subsequently cold-pressed into disks with a 13 mm diameter and ~ 2.5 mm thickness at a uniaxial pressure of 11 MPa and free-sintered in a hydrogen atmosphere at 600 °C for 8 h. An extended time of the reduction procedure was applied to ensure the total decomposition of the PVA, which begins above 300 °C [40]. For comparison, a set of dense polycrystalline samples with the same level of In impurity were produced, as detailed below. First, $\text{In}_x\text{Co}_4\text{Sb}_{12}\text{O}_y$ ($x = 0.1, 0.2, 0.4, 1$) powders were synthesised as described above. Next, the samples were pressed at 11.2 MPa and reduced in hydrogen at 600 °C for 8 h. Then, the samples were ground and subsequently sintered in a graphite die at 550 °C for 5 min at a pressure of 40 MPa using PECS under Ar atmosphere. Disk samples of 10 mm in diameter and ~ 2.5 mm in thickness were obtained to determine the thermal and electrical transport properties. The reaction scheme for both routes is presented in Fig. 2.

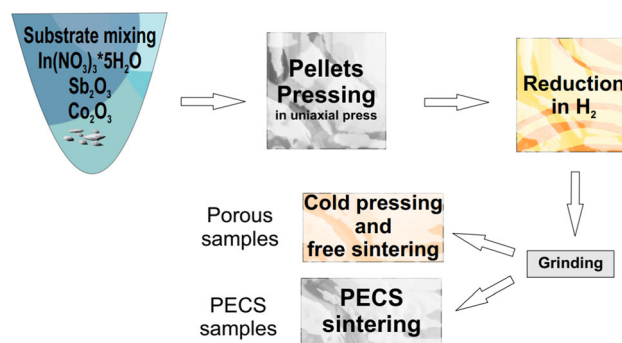


Figure 2 Scheme presenting synthesis process for free-sintered and PECS-sintered samples.

The phase composition of the materials was investigated by the X-ray diffraction (XRD) method (X'Pert Pro MPD Philips diffractometer) using $\text{Cu}_{K\alpha}$ radiation ($\lambda = 1.542 \text{ \AA}$) at room temperature. The XRD patterns were analysed by the LeBail method [41] using the FullProf software. The lattice parameters of the investigated samples were obtained as profile-fitting parameters. Uncertainty was estimated at 0.002 Å, on the basis of the difference between the parameters obtained in different fits. The microstructure and morphology of the investigated materials were analysed using an FEI Quanta FEG 250 scanning electron microscope (SEM) with a secondary electron detector operating in high vacuum mode with an accelerating voltage of 30 kV. A quantitative elemental composition analysis using an energy-dispersive X-ray spectroscopy (EDX) by EDAX Genesis APEX 2i with an ApolloX SDD spectrometer was performed. In order to determine the valence states of the elements, X-ray photoemission spectroscopy (XPS) analyses were performed at room temperature under a pressure below 1.1×10^{-9} mBar. The photoelectrons were excited by an Mg-K α X-ray anode operated at 15 keV and 300 W. An Omicron Argus hemispherical electron analyser with a round aperture of 4 mm was used to analyse the emitted photoelectrons. Measurements were carried out in constant analyser energy (CAE) mode with a pass energy equal to 50 eV. To remove contaminations and oxides, each surface was etched before the measurement. An argon ion gun with an energy up to 5 keV was used for etching for 5 min.

The electrical conductivity and Seebeck coefficient were measured using a direct-current four-probe method (Linseis LSR-3 platform) over the temperature range of 50–500 °C in a helium atmosphere. The

accuracy of the method given by the manufacturer for both parameters is $\pm 5\%$. The charge carrier concentration was determined using a Linseis HCS system. The measurements were performed at room temperature and in an air atmosphere. A series of repeated measurements of the Hall effect revealed a 50% uncertainty of the measurement. Consequently, the obtained results provide information about the order of magnitude of the measured values. Thermal diffusivity α_d was measured by Laser Flash Analysis (LFA 457 MicroFlash, HgCdTe detector, Netzsch GmbH & Co.) under an Ar flow of $30 \text{ cm}^3/\text{min}$ in a temperature range of $50\text{--}400 \text{ }^\circ\text{C}$. The accuracy of the α_d measurement was estimated by the manufacturer to $\pm 5\%$. The densities (ρ) and total porosities of the samples were determined using a hydrostatic method after pore filling with kerosene under vacuum conditions. The estimated accuracy of this measurement is $\pm 5\%$. Thermal conductivity κ was calculated as:

$$\kappa = a_d \cdot c_p \cdot \rho \quad (1)$$

where c_p is the specific heat capacity evaluated from the Dulong–Petit law. The uncertainty of κ values is $\pm 7\%$, and it was estimated from cumulative uncertainty of thermal conductivity components.

The kinetics of the reduction process was investigated by means of TG (thermogravimetric) analysis using a custom-made apparatus. A sample of the reduced material was put in a stainless steel crucible lined with aluminium foil. The crucible was then placed on the top of a stainless steel rod, transferring the load onto a balance (AXIS ALZ120), measuring with a 0.1 mg accuracy. The temperature was measured on top of the rod with a thermocouple placed inside it with a maximum uncertainty equal to 1.6%. The measurements were performed under a $160 \text{ cm}^3/\text{min}$ hydrogen flow. The lower part of the column was cooled. Additionally, silica gel was put in the cooled area of the reaction chamber to capture water vapour. The experiments were performed in nonisothermal conditions, with a $5 \text{ K}/\text{min}$ heating rate, similar to that used for the synthesis, and were performed on milled powders, with the milling procedure being exactly the same as that for the preparation of the samples.

Results and discussion

Optimisation of the reduction process

In order to optimise the process of chemical reduction in oxides, several TG experiments were performed. The selected results of the TG and derivative thermogravimetry (DTG) analyses, both for the pure cobalt and antimony oxides and for their mixtures, are presented in Figs. 3 and 4. The data for Co_2O_3 were multiplied by a factor of 0.25, and 0.75 for Sb_2O_3 , according to the content in the oxide mixture. The reduction in the cobalt oxide initiates at a low temperature of about $180 \text{ }^\circ\text{C}$. This process has two clearly visible steps, corresponding to the two maxima on the DTG curve in Fig. 3a. The first can be assigned to the $\text{Co}_2\text{O}_3 \rightarrow \text{Co}_3\text{O}_4$ reaction (TG curve, Fig. 4). The second can be further divided into two strongly overlapping reactions ($\text{Co}_3\text{O}_4 \rightarrow \text{CoO}$ and $\text{CoO} \rightarrow \text{Co}$). The measured mass change and proposed reduction mechanism are in agreement with the results of others [42–45]. The whole process reaches conversion degree x equal to 92%. The reduction in antimony oxide occurs at a significantly higher temperature, starting at $480 \text{ }^\circ\text{C}$. In the case of this oxide, the measured mass change corresponds to 132% of conversion degree x . This apparent effect is a result of the high volatility of antimony and antimony oxide [46]. However, during the synthesis of CoSb_3 , the Sb loss is expected to be lower, due to the binding of antimony atoms in the compound. In the

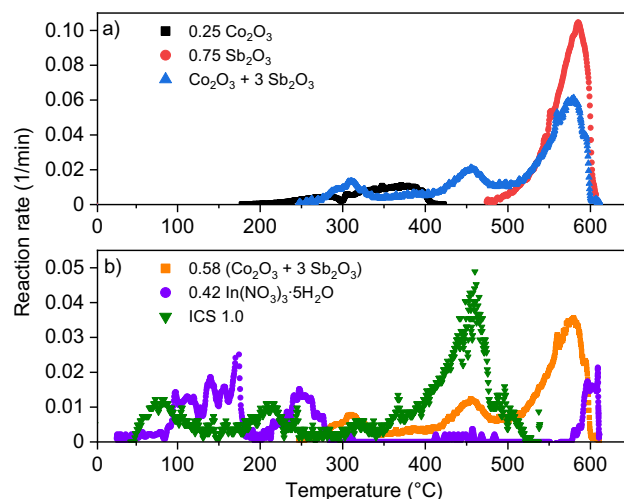


Figure 3 DTG signal (reaction rate) versus the temperature for the reduction in indium(III) nitrate hydrate, Co and Sb oxides in a hydrogen atmosphere.

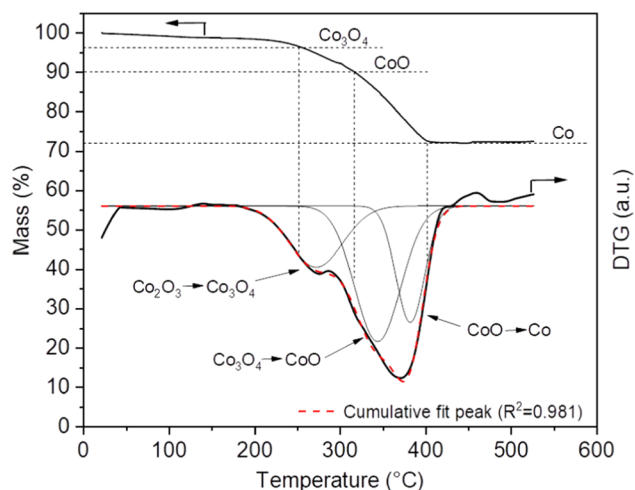


Figure 4 TG and DTG curve of Co_2O_3 reduced in H_2 . Dashed lines correspond to the calculated values of the mass of the sample with a given chemical composition.

case of the mixture of oxides, both steps of cobalt oxide reduction are moved towards higher temperatures. The reduction in cobalt oxide seems to be suppressed by the presence of antimony oxide. Conversion equal to 25% (corresponding to the oxide in Co_2O_3) is reached at 440°C , which is lower than the starting temperature of the pure Sb_2O_3 reduction.

Finally, the reduction in a mixture of oxide materials corresponding to the composition of the product of $\text{InCo}_4\text{Sb}_{12}$ (labelled as ICS10 in Fig. 3) was performed. The reduction process follows the pattern presented in Fig. 3b. Firstly, below 300°C , the $\text{In}(\text{NO}_3)_3 \cdot 5\text{H}_2\text{O}$ decomposes in a few steps into In_2O_3 . A comparison of the plots for the mixtures of oxides with and without $\text{In}(\text{NO}_3)_3 \cdot 5\text{H}_2\text{O}$ (Fig. 3b) indicates that the presence of this compound enhances the reduction in antimony oxide because the corresponding peak in the DTG curve is shifted towards low temperatures. However, a separate peak for cobalt oxide reduction cannot be observed. The reduction in antimony oxide may be partially overlapped by $\text{In}(\text{NO}_3)_3 \cdot 5\text{H}_2\text{O}$. The reduction in Co_2O_3 probably occurs simultaneously with the Sb_2O_3 reduction. The strong influence of the presence of In_2O_3 on the Sb_2O_3 reduction process was confirmed in a separate experiment without Co_2O_3 .

After all of the TG experiments had been performed, a metallic product was found in the crucible. This shows that the reduction in the investigated oxides can be successfully performed. Under measurement conditions, part of the oxide remained

unreacted. However, during the synthesis of the samples, a longer, two-step process was allowed for a complete reduction in the starting materials, which was further confirmed by the XRD structural analysis.

Structural and microstructural analysis

To determine the structure of the materials, XRD measurements were performed on the cold-pressed and PECS-sintered $\text{In}_x\text{Co}_4\text{Sb}_{12}$ ($x = 0.1, 0.2, 0.4, 1$) samples (Fig. 5). The XRD diffraction patterns reveal that all free-sintered $\text{In}_x\text{Co}_4\text{Sb}_{12}$ ($x = 0.1, 0.2, 0.4, 1$) samples contain only a small amount of the CoSb_2 impurity phase. The calculated values of the lattice constant of the main phase are presented in Fig. 6. The expansion of the unit cell with increasing indium content, for $x < 0.4$, confirms that the In is incorporated into the CoSb_3 structure. The lattice constants of the samples with indium content $x = 0.2$ and $x = 0.4$ are close to each other, which is consistent with the EDX quantitative analysis (Table 1). The actual composition of the $\text{In}_1\text{Co}_4\text{Sb}_{12}$ PECS-sintered sample shows a smaller In content. The higher In quantity in the $\text{In}_1\text{Co}_4\text{Sb}_{12}$ free-sintered sample correlates with a more distinguished InSb XRD maximum. The amount of the indium atoms incorporated into the voids is expected to be similar, corresponding to the maximum value. A deficiency of antimony is observed in all of the samples. The Sb deficiency is smaller in the PECS-sintered samples due to the shorter sintering time and is compensated by the presence of an Sb-poor CoSb_2 phase. For the PECS-sintered samples with $x = 0.1, 0.2$, no reflections corresponding to CoSb_2 precipitation were observed in the X-ray diffraction patterns.

Selected SEM images of the porous $\text{In}_x\text{Co}_4\text{Sb}_{12}$ ($x = 0.1, 0.2, 0.4, 1$) materials are shown in Fig. 7. The SEM micrograph of the free-sintered $\text{In}_{0.2}\text{Co}_4\text{Sb}_{12}$ sample shows a highly porous structure with an average grain size in the range of 450–900 nm which also forms agglomerates. The pores are uniformly distributed. Samples with varying indium content did not exhibit significant differences with respect to the sample homogeneity, grain size or grain growth during the process. The major difference was observed in the varying porosities, which is discussed in the following paragraphs. On the other hand, the SEM image of the $\text{In}_{0.2}\text{Co}_4\text{Sb}_{12}$ PECS-sintered sample shows a highly dense structure. A close-

Figure 5 X-ray diffraction patterns of free-sintered and PECS-sintered $\text{In}_x\text{Co}_4\text{Sb}_{12}$ ($x = 0.1, 0.2, 0.4, 1$) samples. Marked reflections correspond to the CoSb_2 and InSb phases.

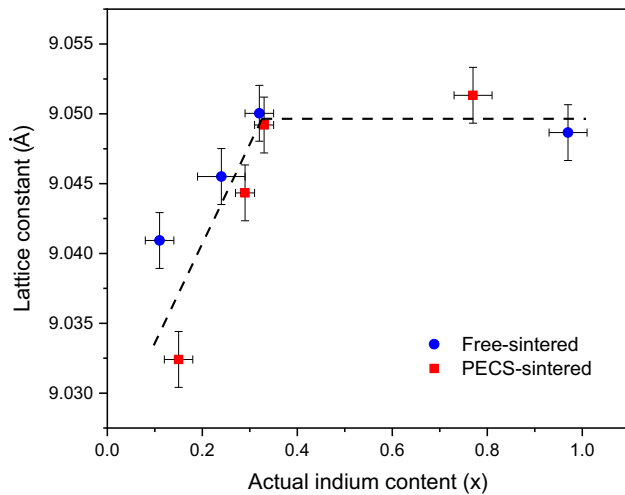
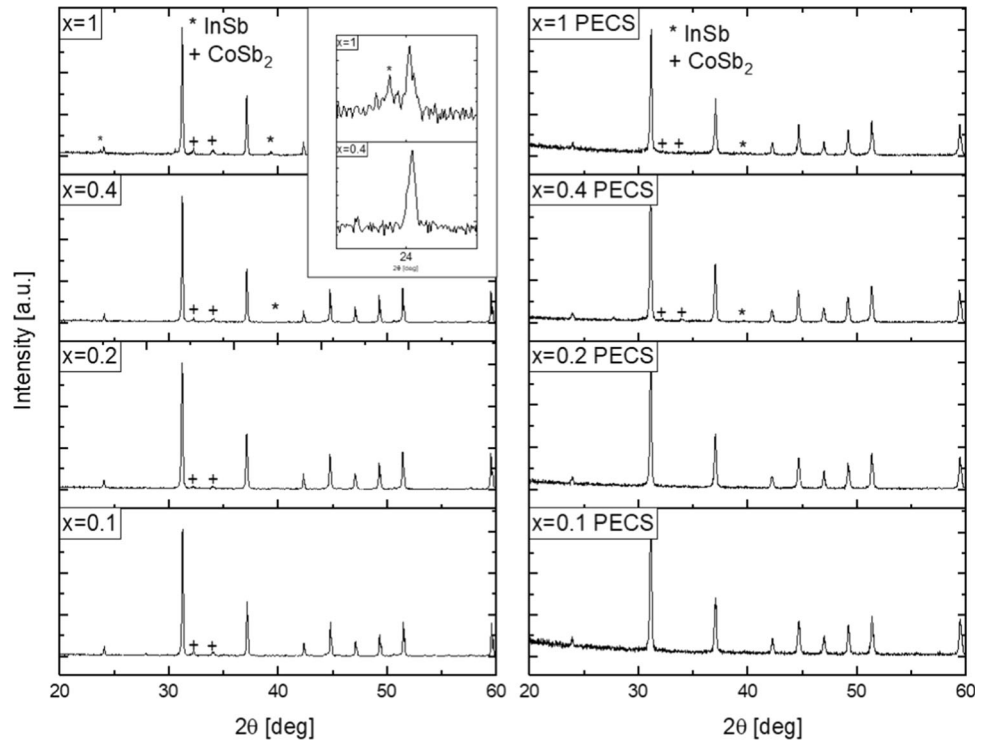


Figure 6 Lattice constant versus the actual amount of indium (x) in the structure of $\text{In}_x\text{Co}_4\text{Sb}_{12}$ prepared by free sintering and PECS sintering. The dashed line is a guide for an eye.

up of the cold-pressed $\text{In}_1\text{Co}_4\text{Sb}_{12}$ SEM image shows the precipitations, marked with circles and arrows, with a size in a range of 40–50 nm, which occur as islands at the grain surface and grain boundary. These precipitations were also found in the $\text{In}_{0.4}\text{Co}_4\text{Sb}_{12}$ sample. The precipitations are believed to be the secondary InSb phase noticeable in the XRD patterns. The formation of a nanometre-sized InSb phase at the

boundaries of the $\text{In}_1\text{Co}_4\text{Sb}_{12}$ grains was previously reported in [20, 42].

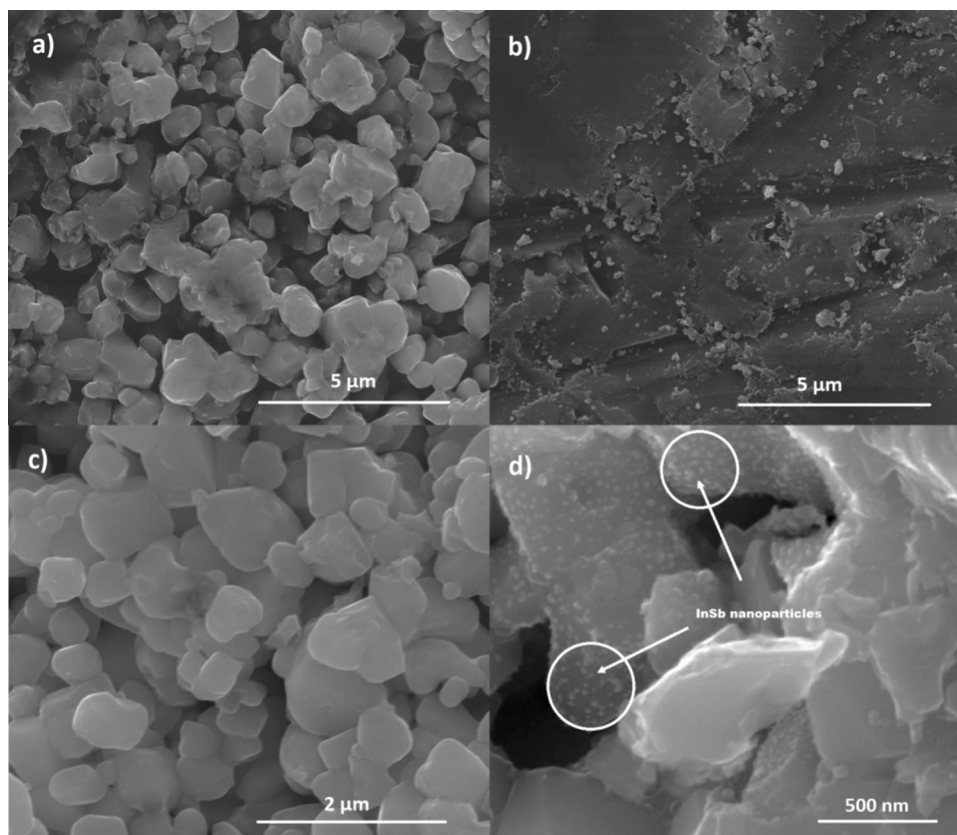
XPS measurement was performed in order to find out whether the oxides were fully reduced. The binding energies were corrected using the background $\text{C}1s$ line (285.0 eV) as a reference. XPS spectra were analysed using a Shirley background subtraction and Gaussian–Lorentzian curve. The results are presented in Fig. 8.

The XPS spectrum for the $\text{In}3d$ region can be fitted by one spin–orbit doublet ($2d_{3/2}$ and $3d_{5/2}$). The position of the $3d_{5/2}$ peak is slightly higher than for In^0 and lower than for the oxide compounds [47, 48]. It could be correlated with an electron transfer to the matrix in the In -filled CoSb_3 [49], confirming the electron-donor character of In atoms. This is in agreement with the covalent character of In – Sb bonding [50]. In the $\text{Co}2p$ region, only the $\text{Co}2p_{3/2}$ line was analysed due to interference with Sb MNN Auger electrons in a higher binding energies region. The recorded binding energy was equal to 777.76 eV, which is close to those previously obtained for filled CoSb_3 [49, 51]. No additional maxima were found between 779 and 781 eV, which are binding energies characteristic for cobalt oxides [52]. In the $\text{Sb}3d$ region, the spectrum can be fitted by only one doublet, similarly to the results presented in [53]. This effect,

Table 1 Porosity, Hall carrier concentration and mobility of the $\text{In}_x\text{Co}_4\text{Sb}_{12}$ ($x = 0.1, 0.2, 0.4, 1$) materials

Nominal composition	EDX area composition	Porosity Φ (%)	Carrier concentration (measured) $\pm 50\%$ (10^{19} cm^{-3})	Carrier concentration (corrected) (10^{19} cm^{-3})	Carrier mobility $\pm 55\%$ ($\text{cm}^2/\text{V s}$)
$\text{In}_{0.1}\text{Co}_4\text{Sb}_{12}$	$\text{In}_{0.11(3)}\text{Co}_4\text{Sb}_{10.6}$	41	– 2.0	3.0	54.8
$\text{In}_{0.2}\text{Co}_4\text{Sb}_{12}$	$\text{In}_{0.24(5)}\text{Co}_4\text{Sb}_{10.8}$	36	– 5.5	7.8	41.5
$\text{In}_{0.4}\text{Co}_4\text{Sb}_{12}$	$\text{In}_{0.32(3)}\text{Co}_4\text{Sb}_{10.2}$	30	– 5.5	7.3	64.8
$\text{In}_1\text{Co}_4\text{Sb}_{12}$	$\text{In}_{0.97(4)}\text{Co}_4\text{Sb}_{11.4}$	28	– 62.0	80.0	6.5
$\text{In}_{0.1}\text{Co}_4\text{Sb}_{12}$ -PECS	$\text{In}_{0.15(3)}\text{Co}_4\text{Sb}_{11.1}$	4.7	– 6.8	7.1	19.3
$\text{In}_{0.2}\text{Co}_4\text{Sb}_{12}$ -PECS	$\text{In}_{0.29(2)}\text{Co}_4\text{Sb}_{11.4}$	5.5	– 4.0	4.2	103.9
$\text{In}_{0.4}\text{Co}_4\text{Sb}_{12}$ -PECS	$\text{In}_{0.33(2)}\text{Co}_4\text{Sb}_{12.4}$	2.5	– 11.4	11.7	31.2
$\text{In}_1\text{Co}_4\text{Sb}_{12}$ -PECS	$\text{In}_{0.77(4)}\text{Co}_4\text{Sb}_{11.3}$	5.4	– 116.0	121.0	4.5

Figure 7 SEM images of the surface of the samples: **a** free-sintered $\text{In}_{0.2}\text{Co}_4\text{Sb}_{12}$, **b** PECS-sintered $\text{In}_{0.2}\text{Co}_4\text{Sb}_{12}$, **c** free-sintered $\text{In}_{0.4}\text{Co}_4\text{Sb}_{12}$, **d** InSb precipitations at the boundaries and on the surface of $\text{In}_1\text{Co}_4\text{Sb}_{12}$ sample grains.



resulting from the different character of Sb bonding, is clearly visible in the XPS spectra presented in [49, 51]. The obtained $\text{Sb}3d_{5/2}$ binding energy is close to that found in [51, 49]. Additionally, the $\text{O}1s$ maximum was present. Because no oxides were found in the material, the oxide found with the XPS can be

assigned to surface contamination. It can be clearly seen that the values of the recorded binding energies of the photoelectrons are close to values characteristic for the elemental (metallic) states for all three measured elements, which is typical for intermetallic

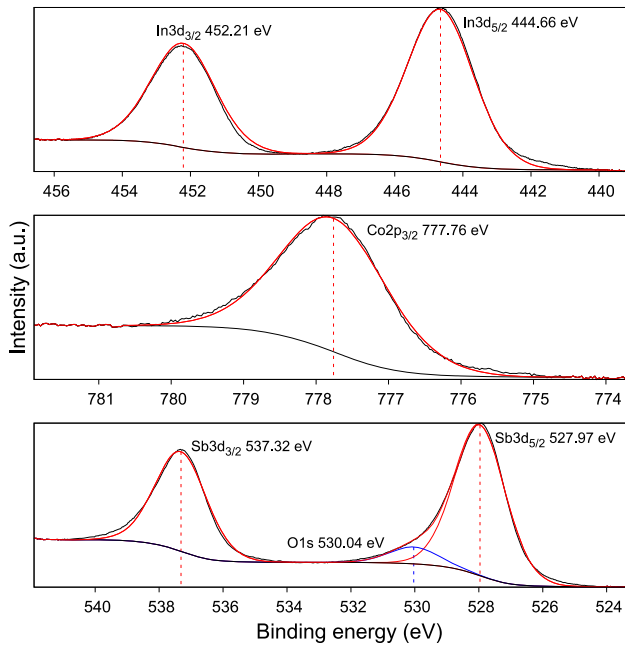


Figure 8 In $3d$, Co $2p_{1/2}$ and Sb $3d$ regions of an XPS spectrum of the In $_1$ Co $_4$ Sb $_{12}$ porous sample.

compounds. It is also typical for covalent bonding with a small charge transfer between atoms [54].

Table 1 contains the results of measurements of the porosity and Hall carrier concentration for the prepared samples. The porosities of the free-sintered samples range from 28 to 41% and decrease with the nominal In content. It is worth noting that despite the exceptionally high porosities, the grains are strongly bonded and thus the samples are not fragile. Variations in the porosities of samples with different nominal In contents could be explained by the presence of the InSb secondary phase, which is likely to form an eutectic at the primary grain surface, which improves grain connectivity during the second sintering [55]. Thus, some undetectable, residual InSb phase may occur in the In $_{0.2}$ Co $_4$ Sb $_{12}$ sample as well.

PECS-sintered materials exhibit lower porosity, ranging from 2.5 to 5.5%. In this case, the correlation between the In content and porosity was not observed. In both cases, samples with the highest indium content have significantly increased carrier concentration. The literature data show different carrier concentrations for similar compositions [5, 56, 57]. The results obtained in this work are comparable to those reported in [56]. All materials show *n*-type semiconductor behaviour. Furthermore, the carrier mobility was calculated on the basis of the charge carrier concentration and electrical

conductivity with porosity correction, with a total uncertainty of 55%. In the case of the conductivity, a standard Bruggeman correction was used. For the carrier concentration, a method proposed by Jurtschke et al. [58] for spherical pores was used. These simplified models result in an additional error in the estimation of the porosity-corrected values, especially in the case of the free-sintered samples. The samples with traces of InSb and CoSb $_2$ phases have different carrier concentrations, but also exhibit differences in carrier mobility which entail electrical conductivity behaviour. The additional phases may impair the electrical conductivity [59]. In the case of the In $_1$ Co $_4$ Sb $_{12}$ samples, the significantly higher carrier concentration is caused by a significant amount of Sb vacancies in the structure, resulting from the measured Sb deficiency and the formation of the InSb phase. These vacancies induce defect bands in the energy gap and can even result in a semimetallic character of the material [52].

Electrical properties

Figure 9 shows the temperature dependence of electrical conductivity (σ) for the In $_x$ Co $_4$ Sb $_{12}$ ($x = 0.1, 0.2, 0.4, 1$) samples with different densities. The samples sintered under pressure using the PECS technique exhibit higher σ values than the free-sintered materials. The σ increases with the increasing indium content, which confirms that the In inside the voids of the crystal structure acts as an electron donor. The

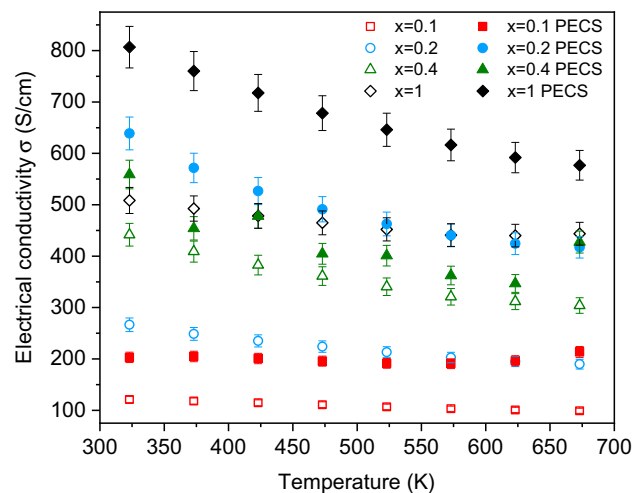


Figure 9 Dependence of the electrical conductivity versus temperature for the cold-pressed and PECS In $_x$ Co $_4$ Sb $_{12}$ ($x = 0.1, 0.2, 0.4, 1$) samples.

highest electrical conductivity is reported for the $\text{In}_x\text{Co}_4\text{Sb}_{12}$ samples, for both free-sintered and PECS-densified materials, which could be explained by the highest carrier concentration. The greater grain connectivity for the composition with lower porosities also alters the conductivity transport for the free-sintered samples. The values of σ for this material are higher than reported previously [12], reaching 806 S/cm for the $\text{In}_1\text{Co}_4\text{Sb}_{12}$ -PECS sample. All samples exhibit the behaviour of heavily doped semiconductors.

The Seebeck coefficient values of the $\text{In}_x\text{Co}_4\text{Sb}_{12}$ ($x = 0.1, 0.2, 0.4, 1$) samples are presented in Fig. 10. The negative Seebeck coefficient of all samples suggests an n-type semiconducting mechanism, which is in agreement with the results of the Hall effect measurements (Table 1). The α of the $\text{In}_{0.1}\text{Co}_4\text{Sb}_{12}$ -PECS reaches $-277 \mu\text{V/K}$ at 470 K. The absolute Seebeck coefficient decreases with the increasing In content. This correlation is in agreement with the charge carrier concentrations of the investigated materials [60]. The InSb secondary phase should not have a significant influence on the Seebeck effect, because its grains do not form a continuous structure. The $\text{In}_{0.1}\text{Co}_4\text{Sb}_{12}$ and $\text{In}_{0.2}\text{Co}_4\text{Sb}_{12}$ samples, both free-sintered and PECS-sintered, exhibit an upturn in their $\alpha(T)$ dependence. This behaviour is probably caused by the bipolar conduction, where thermal excitation of the electrons over the band gap causes the formation of holes in the valence band. A similar dependence was observed by Sesselmann et al. [19]. The

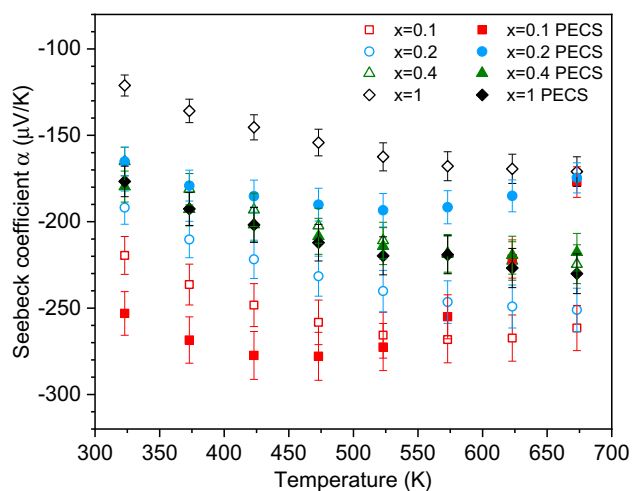


Figure 10 Dependence of the Seebeck coefficient versus temperature for the free-sintered and PECS $\text{In}_x\text{Co}_4\text{Sb}_{12}$ ($x = 0.1, 0.2, 0.4, 1$) samples.

phenomenon occurred in filled skutterudites with a small indium content ($x = 0.05$), which may indicate that the real indium content of these samples is smaller than the nominal one. Li et al. [18] observed this phenomenon in all samples ($x = 0.05\text{--}0.4$); however, in the $\text{In}_{0.05}\text{Co}_4\text{Sb}_{12}$ sample, the upturn was significant.

According to the previous research [59], Seebeck coefficient values are inversely proportional to the carrier mobility in porous materials. In the case of our materials, we find this dependence to be true as well. In a single parabolic band model, the Seebeck coefficient is directly proportional to the effective mass. In turn, the effective mass is inversely proportional to the mobility of the carriers, which gives the $\alpha \sim 1/\mu$ relation. The mobility in the investigated porous materials is higher than in the corresponding dense PECS samples, and the absolute value of the Seebeck coefficient for samples with pores is smaller.

Thermal conductivity

The measured values of thermal conductivities κ of the $\text{In}_x\text{Co}_4\text{Sb}_{12}$ (0.1, 0.2, 0.4, 1) samples are shown in Fig. 11. At the low-temperature range, κ decreases with the increasing temperature, and at 520 K, starts to increase with the increasing temperature. Many research results indicate that the lowest lattice thermal conductivity is observed for the filled skutterudites with the highest indium content [12, 18, 19, 61]. However, in our research, the lowest total thermal

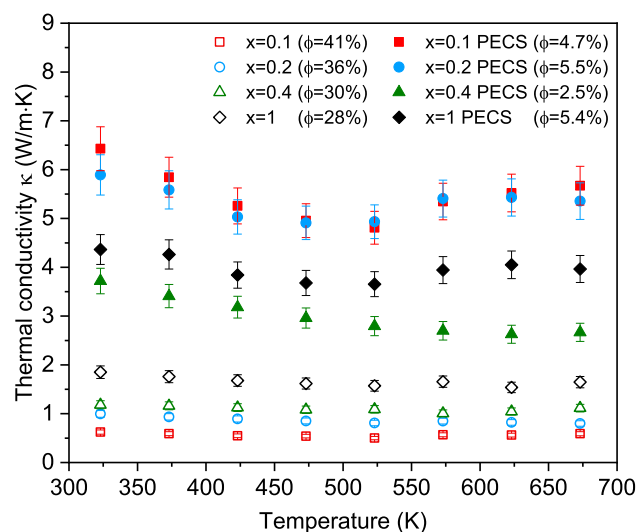


Figure 11 Thermal conductivity versus temperature for the free-sintered and PECS $\text{In}_x\text{Co}_4\text{Sb}_{12}$ ($x = 0.1, 0.2, 0.4, 1$) samples.

conductivity is obtained for the free-sintered $\text{In}_{0.1}\text{Co}_4\text{Sb}_{12}$ sample (0.5 W/m K at 523 K). In this case, the material exhibits the highest porosity (41%), which seems to have the greatest impact on the decrease in the thermal conductivity.

Analyses of heat transport in composites and porous thermoelectric materials have been widely reported [62–66]. The commonly applied effective media theory (EMT) [67] is a very useful tool for predicting the value of the thermal or electrical conductivity of a composite using the properties and content of its components. The most complex models can take into account, for example, the presence of microcracks [68], the type of gas inside the pores, the radiative contribution to the thermal conductivity [69], the presence of open porosity [69] or a porosity system consisting of various types of pores [70–72]. We have focused only on the application of effective media theory to the thermal conductivity. One of the assumptions of EMT is that components maintain their properties in a composite (i.e. porous material). In our case, the two preparation procedures (free sintering in hydrogen and PECS) of the same material result in different electrical properties, which are presented in Table 1. Thus, the application of effective media theory for electrical conductivity is not possible in this case. It is also important to mention that for heterogeneous media (i.e. porous materials), there are difficulties in the calculation of the electrical and lattice components of the thermal conductivity. The current state of knowledge does not contain a reliable method of estimating the Lorenz number for these materials; thus, the application of the Wiedemann–Franz law in this case is not trivial.

For a better understanding of the influence of porosity on the reduction in thermal conductivity, the experimental results were compared with selected generally used theoretical models for open porosity. All of the models applied in our analysis assume that (a) all pores are of identical shape, (b) radiation inside the pores can be neglected and thus its contribution to the total thermal conductivity can be omitted ($T < 350$ K), (c) the shape of the pores can be described by a sphere or spheroid and (d) each single pore is embedded in a continuous matrix. One of the simplest models was created by Maxwell [73]:

$$\frac{\kappa_c}{\kappa_m} = \left(1 - \frac{3}{2}f\right) \tag{2}$$

where κ_c and κ_m are the thermal conductivities of the porous material and the matrix, respectively, and f is the volume fraction of the porosity. In fact, this model should be applied only for materials with $f < 0.1$ and assumes a spherical shape of the pores. More advanced models are based on the Maxwell model and also take into account different pore shapes (eg. lamellae, cylinders, spheroids).

One of the most commonly used is the Bruggeman model [74]:

$$\frac{\kappa_c}{\kappa_m} = (1 - f)^X \tag{3}$$

$$X = \frac{1 - (\cos \beta)^2}{1 - F} + \frac{(\cos \beta)^2}{2F} \tag{4}$$

where β is the angle between the heat flux direction and the rotational axis of the spheroid [75], and F is shape factor of the spheroid, described by the formula:

$$F = \frac{1}{2} \left(1 - \frac{1}{1 + 1.6\frac{a}{c} + 0.4\left(\frac{a}{c}\right)^2}\right) \tag{5}$$

and also presented graphically and described in more detail in Fig. 12. It should be noted that, for boundary conditions $F = 0$ and $F = 0.5$, Eqs. (3)–(5) can describe lamellae and cylinders, respectively. The Bruggeman model can characterise materials with the whole range of a volumetric fraction of the pores ($0 < f < 1$). Equation (4) is used for the particular case when all pores are oriented identically in relation to the heat

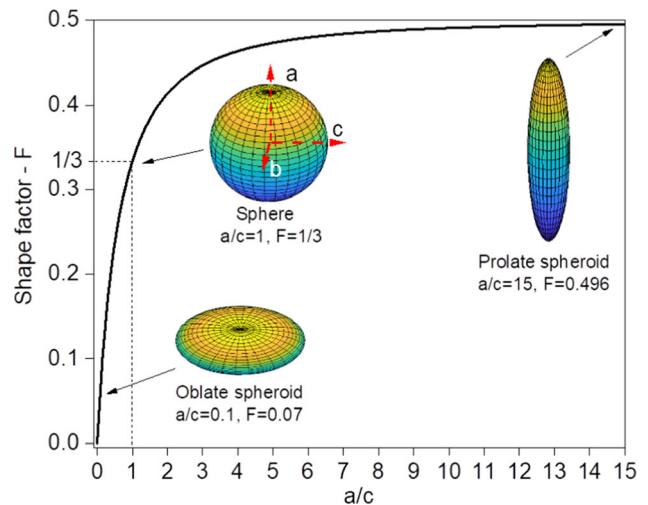


Figure 12 Shape factor F for a spheroid pore with axes a , b , and c (where $b = c$) calculated as a function of the a/c ratio, where a is a rotational axis of the spheroid.

flux direction. For the more general situation of randomly oriented pores, Eq. (4) can be rewritten as follows [76]:

$$X = \frac{1}{3} \left(\frac{1}{2F} + \frac{2}{1-F} \right) \quad (6)$$

For a visualisation of how the κ_c/κ_m values change according to the Bruggeman model for various shapes and orientations of porosity, please refer to the Mendeley Data Repository [77]. Meredith and Tobias [76] proposed a similar model for randomly oriented spheroidal-shaped porosity:

$$\frac{\kappa_c}{\kappa_m} = \left[\frac{2-f}{2+(X-1)f} \right] \cdot \left[\frac{2(1-f)}{2(1-f)+Xf} \right] \quad (7)$$

Theoretical values of the $\frac{\kappa_c}{\kappa_m}$ ratio calculated for selected models and experimental values are presented in Fig. 13. For experimental data, the thermal conductivity of matrix κ_m (perfectly dense material) was estimated for each composition by linear regression on two values of κ —for the sample prepared by free sintering and by the PECS method. κ_m was assumed as coefficient b from the obtained equation of the line $y = ax + b$, where y is the thermal conductivity and x is the porosity (%). For the purpose of this estimation, an assumption was made that porosity is the main factor affecting the change in thermal conductivity. The low porosity of the PECS samples allowed the matrix thermal conductivities to

be correctly estimated, which are presented in Table 2.

Theoretical values of $\frac{\kappa_c}{\kappa_m}$ for sphere-shaped pores are marked with a dashed line, while the solid lines represent the results for spheroidal pores. The corresponding values of shape factor F are also given. It is clear that the models where the pores are assumed to be sphere-shaped do not describe well the experimental data which is in agreement with the SEM analysis. In Fig. 7a, c, we can observe a large number of pores, but their shapes are far from perfect spheres. The Bruggeman model considering randomly oriented pores in the shape of a prolate spheroid (green solid line) also does not fit the sample data. This suggests that in the case of $\text{In}_x\text{Co}_4\text{Sb}_{12}$ prepared by free sintering, cylindrical or cigar-shaped pores are rare. Without a doubt, models that assume the majority of pores are in the shape of an oblate spheroid (back and red solid lines) describe experimental data the best. Additionally, an area around the black line is presented to visualise the range of values of shape factor that correspond to the experimental data. The largest F values of this area are 0.04 and 0.07, which correlate to a/c ratios of 0.05 and 0.1, respectively. Between the Bruggeman model and the Meredith and Tobias model, the more accurate in this case is the former. These curves were fitted to the experimental points using the least square method. For the Bruggeman model, the square of correlation coefficient $R^2 = 0.94$, and for the Meredith and Tobias model, $R^2 = 0.89$.

Interestingly, both models are in agreement with the shape of porosity—oblate pores with relatively similar values of the shape factor.

Thermoelectric figure of merit

The calculated ZT values are shown in Fig. 14. The highest ZT value is observed for the free-sintered $\text{In}_{0.2}\text{Co}_4\text{Sb}_{12}$ sample ($ZT = 1$ at 673 K). In many samples, the figure of merit increases with the temperature, and at around 500 K, reaches a plateau. The high ZT values remain almost constant across a wide range of temperatures, which is interesting considering the use of the material in thermoelectric modules.

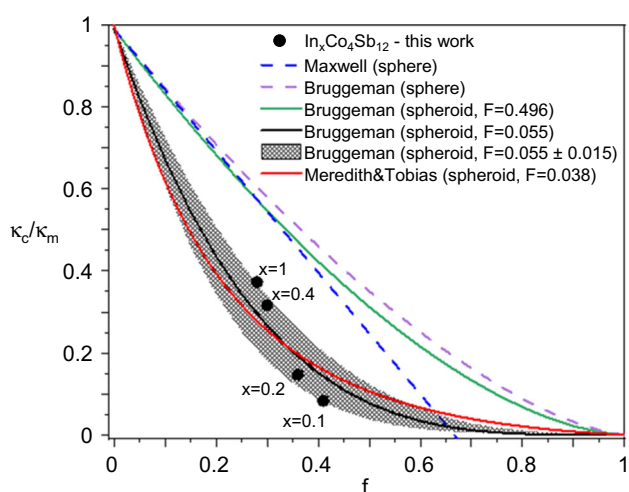
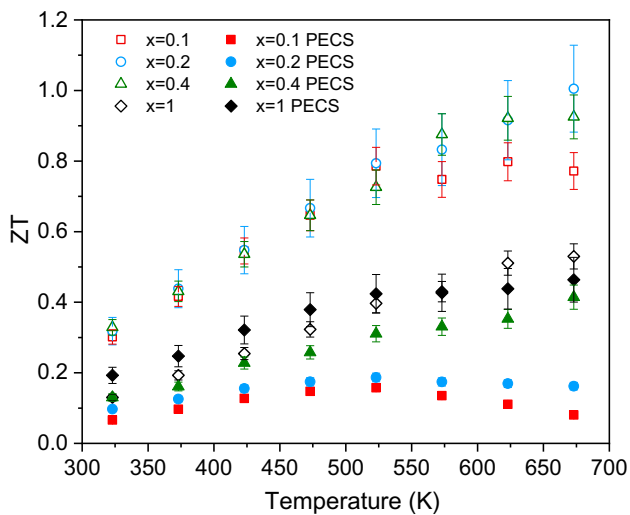


Figure 13 Experimental values of κ_c/κ_m and theoretical models as a function of the volumetric fraction of porosity (f) for different pore shapes. All models in this graph with spheroid-shaped porosity assume its random orientation in the material.

Table 2 Approximated values of the thermal conductivity of each material without any porosity

Nominal composition	The estimated value of κ of the material with 0% porosity [W/(m K)]
$\text{In}_{0.1}\text{Co}_4\text{Sb}_{12}$	7.18
$\text{In}_{0.2}\text{Co}_4\text{Sb}_{12}$	6.77
$\text{In}_{0.4}\text{Co}_4\text{Sb}_{12}$	3.95
$\text{In}_1\text{Co}_4\text{Sb}_{12}$	4.96

**Figure 14** Thermoelectric figure of merit ZT versus temperature for the cold-pressed and PECS $\text{In}_x\text{Co}_4\text{Sb}_{12}$ ($x = 0.1, 0.2, 0.4, 1$) samples. The values of uncertainty were calculated using the exact differential method. For the two samples with the lowest values of ZT , the uncertainty bars are smaller than the symbols.

Conclusions

In-filled CoSb_3 skutterudites were synthesised using the oxide reduction method. A basic kinetic analysis of this process revealed that it can be successfully performed in temperatures even lower than the reduction in single element oxides. The obtained materials had a large amount of porosity ($\sim 40\%$) that maintains attractive thermoelectric properties. They were also homogeneous except for a very small amount of InSb secondary-phase nano-inclusions. For comparison, high-density samples were prepared using the PECS technique. The significant role of porosity on a decrease in the thermal conductivity of the fabricated material is presented. The thermal conductivity of porous materials is significantly decreased (0.50 W/m K at 523 K for $\text{In}_{0.1}\text{Co}_4\text{Sb}_{12}$, 41% porosity). Samples with higher porosities exhibit lower values of electrical conductivity, but the benefit of lower thermal conductivity outweighs losses in σ , resulting in higher ZT values. The highest ZT was

obtained for a porous $\text{In}_{0.2}\text{Co}_4\text{Sb}_{12}$ sample ($ZT = 1$ at 673 K). Experimental values of thermal conductivity were analysed using the effective media theory of heat transport in porous media. The best correlation between the theoretical and measured values is seen by the Bruggeman, and Meredith and Tobias models. The calculations showed that the assumption of randomly orientated pores with a shape of oblate spheroids best fits the experimental data and also corresponds with the observed microstructure of the material.

Materials in which 41% of the volume consists of pores while still showing higher ZT parameters than dense samples could be very serious candidates for the production of cheaper and more efficient TE modules.

Acknowledgements

This work was supported by the National Science Centre Poland (Grant No. 2016/21/B/ST8/03193) and partially by the “New approach for development of efficient materials for direct conversion of heat into electricity” project which is being carried out within the TEAM-TECH (Grant No. 2016-2/14) program of the Foundation for Polish Science co-financed by the European Union under the European Regional Development Fund. The beneficiary of this project is The Lukasiewicz Research Network - Cracow Institute of Technology (Poland).

Open Access This article is licensed under a Creative Commons Attribution 4.0 International License, which permits use, sharing, adaptation, distribution and reproduction in any medium or format, as long as you give appropriate credit to the original author(s) and the source, provide a link to the Creative Commons licence, and indicate if changes were made. The images or other third party material in this article are included in the article’s Creative Commons licence, unless indicated otherwise in a credit line to the material. If material is not included in the article’s

Creative Commons licence and your intended use is not permitted by statutory regulation or exceeds the permitted use, you will need to obtain permission directly from the copyright holder. To view a copy of this licence, visit <http://creativecommons.org/licenses/by/4.0/>.

References

- [1] Tang Y, Hanus R, Chen SW, Snyder GJ (2015) Solubility design leading to high figure of merit in low-cost Ce-CoSb₃ skutterudites. *Nat Commun* 6:1–7. <https://doi.org/10.1038/ncomms8584>
- [2] Morelli DT, Meisner GP, Chen B et al (1997) Cerium filling and doping of cobalt triantimonide. *Phys Rev B Condens Matter Mater Phys* 56:7376–7383. <https://doi.org/10.1103/PhysRevB.56.7376>
- [3] Tang Y, Chen S, Snyder GJ (2015) Temperature dependent solubility of Yb in Yb–CoSb₃ skutterudite and its effect on preparation, optimization and lifetime of thermoelectrics. *J Mater* 1:75–84. <https://doi.org/10.1016/j.jmat.2015.03.008>
- [4] Jelínek M, Zeipl R, Kocourek T et al (2015) Study of Yb-doped CoSb₃ thermoelectric thin films prepared by laser. *Appl Mech Mater* 749:46–50. <https://doi.org/10.4028/www.scientific.net/AMM.749.46>
- [5] Benyahia M, Ohorodniichuk V, Leroy E et al (2018) High thermoelectric figure of merit in mesostructured In_{0.25}Co₄Sb₁₂ n-type skutterudite. *J Alloys Compd* 735:1096–1104. <https://doi.org/10.1016/j.jallcom.2017.11.195>
- [6] Sofo JO, Mahan GD (1998) Electronic structure of CoSb₃: a narrow-band-gap semiconductor. *Phys Rev B* 58:15620–15623. <https://doi.org/10.1103/PhysRevB.58.15620>
- [7] Nolas GS, Morelli DT, Tritt TM (1999) SKUTTERUDITES: a phonon-glass-electron crystal approach to advanced thermoelectric energy conversion applications. *Annu Rev Mater Sci* 29:89–116. <https://doi.org/10.1146/annurev.matsci.29.1.89>
- [8] Pei YZ, Yang J, Chen LD et al (2009) Improving thermoelectric performance of caged compounds through light-element filling. *Appl Phys Lett* 95:10–13. <https://doi.org/10.1063/1.3182800>
- [9] Zhang J, Xu B, Wang LM et al (2012) High-pressure synthesis of phonon-glass electron-crystal featured thermoelectric Li_xCo₄Sb₁₂. *Acta Mater* 60:1246–1251. <https://doi.org/10.1016/j.actamat.2011.10.059>
- [10] Chen LD, Kawahara T, Tang XF et al (2001) Anomalous barium filling fraction and n-type thermoelectric performance of Ba_yCo₄Sb₁₂. *J Appl Phys* 90:1864–1868. <https://doi.org/10.1063/1.1388162>
- [11] Dahal T, Jie Q, Joshi G et al (2014) Thermoelectric property enhancement in Yb-doped n-type skutterudites Yb_xCo₄Sb₁₂. *Acta Mater* 75:316–321. <https://doi.org/10.1016/j.actamat.2014.05.019>
- [12] Khovaylo VV, Korolkov TA, Voronin AI et al (2017) Rapid preparation of In_xCo₄Sb₁₂ with a record-breaking ZT = 1.5: the role of the In overfilling fraction limit and Sb overstoichiometry. *J Mater Chem A* 5:3541–3546. <https://doi.org/10.1039/c6ta09092c>
- [13] Yang J, Stabler FR (2009) Automotive applications of thermoelectric materials. *J Electron Mater* 38:1245–1251. <https://doi.org/10.1007/s11664-009-0680-z>
- [14] Yang J, Caillat T (2006) Thermoelectric materials for space and automotive power generation. *MRS Bull* 31:224–229
- [15] Bötner H Survey on status and trends of thermoelectrics in Europe. In: 3rd conference thermoelectrics goes automotive. Berlin
- [16] Leblanc S, Yee SK, Scullin ML et al (2014) Material and manufacturing cost considerations for thermoelectrics. *Renew Sustain Energy Rev* 32:313–327. <https://doi.org/10.1016/j.rser.2013.12.030>
- [17] LeBlanc S (2014) Thermoelectric generators: linking material properties and systems engineering for waste heat recovery applications. *Sustain Mater Technol* 1:26–35. <https://doi.org/10.1016/j.susmat.2014.11.002>
- [18] Li G, Kurosaki K, Ohishi Y et al (2013) Thermoelectric properties of indium-added skutterudites In_xCo₄Sb₁₂. *J Electron Mater* 42:1463–1468. <https://doi.org/10.1007/s11664-012-2290-4>
- [19] Sesselmann A, Dasgupta T, Kelm K et al (2011) Transport properties and microstructure of indium-added cobalt-antimony-based skutterudites. *J Mater Res* 26:1820–1826. <https://doi.org/10.1557/jmr.2011.102>
- [20] Li H, Su X, Tang X et al (2017) Grain boundary engineering with nano-scale InSb producing high performance In_xCe_yCo₄Sb_{12+z} skutterudite thermoelectrics. *J Mater* 3:273–279. <https://doi.org/10.1016/j.jmat.2017.07.003>
- [21] Alleno E, Chen L, Chubilleau C et al (2010) Thermal conductivity reduction in CoSb₃–CeO₂ nanocomposites. *J Electron Mater* 39:1966–1970. <https://doi.org/10.1007/s11664-009-1043-5>
- [22] Li H, Tang X, Zhang Q, Uher C (2008) Rapid preparation method of bulk nanostructured Yb_{0.3}Co₄Sb_{12+y} compounds and their improved thermoelectric performance. *Appl Phys Lett* 93:2006–2009. <https://doi.org/10.1063/1.3054158>
- [23] Biswas K, Muir S, Subramanian MA (2011) Rapid microwave synthesis of indium filled skutterudites: an energy efficient route to high performance thermoelectric materials.

- Mater Res Bull 46:2288–2290. <https://doi.org/10.1016/j.materresbull.2011.08.058>
- [24] Pourghahramani P, Forssberg E (2007) Reduction kinetics of mechanically activated hematite concentrate with hydrogen gas using nonisothermal methods. *Thermochim Acta* 454:69–77. <https://doi.org/10.1016/j.tca.2006.12.023>
- [25] Rodriguez JA, Hanson JC, Frenkel AI et al (2002) Experimental and theoretical studies on the reaction of H₂ with NiO: role of O vacancies and mechanism for oxide reduction. *J Am Chem Soc* 124:346–354. <https://doi.org/10.1021/ja0121080>
- [26] Juarez JC, Morales R (2008) Reduction kinetics of Ag₂MoO₄ by hydrogen. *Metall Mater Trans B Process Metall Mater Process Sci* 39:738–745. <https://doi.org/10.1007/s11663-008-9173-3>
- [27] Bochentyn B, Karczewski J, Miruszewski T, Kusz B (2015) Structure and thermoelectric properties of Bi–Te alloys obtained by novel method of oxide substrates reduction. *J Alloys Compd* 646:1124–1132. <https://doi.org/10.1016/j.jallcom.2015.06.127>
- [28] Trawiński B, Bochentyn B, Gostkowska N et al (2018) Structure and thermoelectric properties of bismuth telluride—carbon composites. *Mater Res Bull* 99:10–17. <https://doi.org/10.1016/j.materresbull.2017.10.043>
- [29] Bochentyn BM, Karczewski JL, Miruszewski T, Kusz B (2015) Novel method for metal—oxide glass composite fabrication for use in thermoelectric devices. *Mater Res Bull* 76:195–204. <https://doi.org/10.1016/j.materresbull.2015.12.018>
- [30] Bochentyn B, Miruszewski T, Karczewski J, Kusz B (2016) Thermoelectric properties of bismuth-antimony-telluride alloys obtained by reduction of oxide reagents. *Mater Chem Phys* 177:353–359. <https://doi.org/10.1016/j.matchemphys.2016.04.039>
- [31] Lee G, Ha G (2014) Synthesis of Bi_{0.5}Sb_{1.5}Te₃ thermoelectric powder using an oxide-reduction process. *J Electron Mater* 43:1697–1702. <https://doi.org/10.1007/s11664-013-2846-y>
- [32] Kusz B, Miruszewski T, Bochentyn B, Karczewski J (2016) Structure and thermoelectric properties of Te–Ag–Ge–Sb (TAGS) materials obtained by reduction of melted oxide substrates. *J Electron Mater* 45:2–4. <https://doi.org/10.1007/s11664-015-4251-1>
- [33] Lee G, Park B, Kim W et al (2010) Synthesis of Bi–Te–Se-based thermoelectric powder by an oxide-reduction process. *Electron Mater Lett* 6:123–127. <https://doi.org/10.3365/eml.2010.09.123>
- [34] Lim YS, Wi S, Lee G (2017) Synthesis of n-type Bi₂Te_{1-x}Se_x compounds through oxide reduction process and related thermoelectric properties. *J Eur Ceram Soc* 37:3361–3366. <https://doi.org/10.1016/j.jeurceramsoc.2017.04.020>
- [35] Gostkowska N, Miruszewski T, Trawiński B et al (2017) Structure and thermoelectric properties of Cs–Bi–Te alloys fabricated by different routes of reduction of oxide reagents. *Solid State Sci* 73:41–50. <https://doi.org/10.1016/j.solidstateciences.2017.07.016>
- [36] Khan A, Saleemi M, Johnsson M et al (2014) Fabrication, spark plasma consolidation, and thermoelectric evaluation of nanostructured CoSb₃. *J Alloys Compd* 612:293–300. <https://doi.org/10.1016/j.jallcom.2014.05.119>
- [37] Kim SH, Kim MC, Kim MS et al (2016) Nanophase oxalate precursors of thermoelectric CoSb₃ by controlled coprecipitation predicted by thermodynamic modeling. *Adv Powder Technol* 27:773–778. <https://doi.org/10.1016/j.apt.2016.03.006>
- [38] Wu CF, Wei TR, Sun FH, Li JF (2017) Nanoporous PbSe–SiO₂ thermoelectric composites. *Adv Sci*. <https://doi.org/10.1002/adv.201700199>
- [39] Yang H, Wen P, Zhou X et al (2019) Enhanced thermoelectric performance of Te-doped skutterudite with nano-micro-porous architecture. *Scr Mater* 159:68–71. <https://doi.org/10.1016/j.scriptamat.2018.09.015>
- [40] Peng Z, Kong LX (2007) A thermal degradation mechanism of polyvinyl alcohol/silica nanocomposites. *Polym Degrad Stab* 92:1061–1071. <https://doi.org/10.1016/j.polymdegradstab.2007.02.012>
- [41] LeBail A (2005) Whole powder pattern decomposition methods and applications. *Powder Diffr* 20:316–326. <https://doi.org/10.1154/1.2135315>
- [42] Sabat KC, Paramguru RK, Pradhan S, Mishra BK (2015) Reduction of cobalt oxide (Co₃O₄) by low temperature hydrogen plasma. *Plasma Chem Plasma Process* 35:387–399. <https://doi.org/10.1007/s11090-014-9602-9>
- [43] Galleos NG, Porto Lopez JM (1988) Kinetic study of cobalt oxides reduction by hydrogen. *Mater Chem Phys* 19:431–446
- [44] Bulavchenko OA, Cherepanova SV, Tsybulya SV (2009) In situ XRD investigation of Co₃O₄ reduction. *Zeitschrift fur Krist Suppl* 30:329–334. <https://doi.org/10.1524/zksu.2009.0048>
- [45] Ishchenko AV, Bulavchenko OA, Cherepanova SV et al (2009) In situ XRD study of nanocrystalline cobalt oxide reduction. *Kinet Catal* 50:192–198. <https://doi.org/10.1134/s0023158409020086>
- [46] Chernogorenko VB, Lynchak KA, Klimak ZA, Morozova RA (1978) Kinetics of antimony trioxide reduction by hydrogen. Effect of atomic hydrogen. *Sov Powder Metall Met Ceram* 17:419–421. <https://doi.org/10.1007/BF00795791>

- [47.] Das R, Soni RK (2017) Synthesis and surface-enhanced Raman scattering of indium nanotriangles and nanowires. *RSC Adv* 7:32255–32263. <https://doi.org/10.1039/C7RA03317F>
- [48.] Detweiler ZM, Wulfsberg SM, Frith MG et al (2016) The oxidation and surface speciation of indium and indium oxides exposed to atmospheric oxidants. *Surf Sci* 648:188–195. <https://doi.org/10.1016/J.SUSC.2015.10.026>
- [49.] Leszczyński J, Szczyпка W, Candolfi C et al (2017) HPHT synthesis of highly doped $\text{In}_x\text{Co}_4\text{Sb}_{12}$ —experimental and theoretical study. *J Alloys Compd* 727:1178–1188. <https://doi.org/10.1016/J.JALLCOM.2017.08.194>
- [50.] Zhao W, Wei P, Zhang Q et al (2015) Multi-localization transport behaviour in bulk thermoelectric materials. *Nat Commun* 6:6197. <https://doi.org/10.1038/ncomms7197>
- [51.] Zhao W, Wei P, Zhang Q et al (2009) Enhanced thermoelectric performance in barium and indium double-filled skutterudite bulk materials via orbital hybridization induced by indium filler. *J Am Chem Soc* 131:3713–3720. <https://doi.org/10.1021/ja8089334>
- [52.] Dupin J, Gonbeau D, Benqilou-Moudden H et al (2001) XPS analysis of new lithium cobalt oxide thin-films before and after lithium deintercalation. *Thin Solid Films* 384:23–32. [https://doi.org/10.1016/S0040-6090\(00\)01802-2](https://doi.org/10.1016/S0040-6090(00)01802-2)
- [53.] Grosvenor AP, Cavell RG, Mar A (2006) X-ray photoelectron spectroscopy study of the skutterudites $\text{LaFe}_4\text{Sb}_{12}$, $\text{CeFe}_4\text{Sb}_{12}$, CoSb_3 , and CoP_3 . *Phys Rev B* 74:125102. <https://doi.org/10.1103/PhysRevB.74.125102>
- [54.] Anno H, Matsubara K, Caillat T, Fleurial JP (2000) Valence-band structure of the skutterudite compounds CoAs_3 , CoSb_3 , and RhSb_3 studied by x-ray photoelectron spectroscopy. *Phys Rev B Condens Matter Mater Phys* 62:10737–10743. <https://doi.org/10.1103/PhysRevB.62.10737>
- [55.] Eilertsen J, Li J, Rouvimov S, Subramanian MA (2011) Thermoelectric properties of indium-filled $\text{In}_x\text{Rh}_4\text{Sb}_{12}$ skutterudites. *J Alloys Compd* 509:6289–6295. <https://doi.org/10.1016/j.jallcom.2011.03.057>
- [56.] Wang L, Cai KF, Wang YY et al (2009) Thermoelectric properties of indium-filled skutterudites prepared by combining solvothermal synthesis and melting. *Appl Phys A Mater Sci Process* 97:841–845. <https://doi.org/10.1007/s00339-009-5329-5>
- [57.] Tang Y, Qiu Y, Xi L et al (2014) Phase diagram of In–Co–Sb system and thermoelectric properties of In-containing skutterudites. *Energy Environ Sci* 7:812–819. <https://doi.org/10.1039/c3ee43240h>
- [58.] Juretschke HJ, Landauer R, Swanson JA (1956) Hall effect and conductivity in porous media. *J Appl Phys* 27:838–839
- [59.] Gayner C, Prakash D, Ballal A (2017) Influence of secondary phase dispersants and porosity on thermoelectric properties of $\beta\text{-Fe}_{0.91}\text{Mn}_{0.09}\text{Si}_2$. *J Alloys Compd* 698:164–169. <https://doi.org/10.1016/j.jallcom.2016.12.253>
- [60.] Hu C, Zeng X, Liu Y et al (2017) Effects of partial La filling and Sb vacancy defects on CoSb_3 skutterudites. *Phys Rev B* 95:165204. <https://doi.org/10.1103/PhysRevB.95.165204>
- [61.] Visnow E, Heinrich CP, Schmitz A et al (2015) On the true indium content of In-filled skutterudites. *Inorg Chem* 54:7818–7827. <https://doi.org/10.1021/acs.inorgchem.5b00799>
- [62.] Cernuschi F, Ahmaniemi S, Vuoristo P, Mäntylä T (2004) Modelling of thermal conductivity of porous materials: application to thick thermal barrier coatings. *J Eur Ceram Soc* 24:2657–2667. <https://doi.org/10.1016/j.jeurceramsoc.2003.09.012>
- [63.] Muta H, Kurosaki K, Uno M, Yamanaka S (2003) Thermoelectric properties of constantan/spherical SiO_2 and Al_2O_3 particles composite. *J Alloys Compd* 359:326–329. [https://doi.org/10.1016/S0925-8388\(03\)00295-0](https://doi.org/10.1016/S0925-8388(03)00295-0)
- [64.] Chen T-G, Yu P, Chou R-H, Pan C-L (2010) Phonon thermal conductivity suppression of bulk silicon nanowire composites for efficient thermoelectric conversion. *Opt Express* 18:A467–A476. <https://doi.org/10.1364/oe.18.00a467>
- [65.] Umarji AM, Ordonez-Miranda J, Wu Y et al (2018) Particle size effect on the thermal conductivity reduction of silicon based thermoelectric composites. *Sustain Energy Fuels* 2:1764–1771. <https://doi.org/10.1039/c8se00131f>
- [66.] Wu CA, Chang KC, Lin FH et al (2019) Low thermal conductivity and enhanced zT values of porous and nanostructured $\text{Cu}_{1-x}\text{Ni}_x$ alloys. *Chem Eng J* 368:409–416. <https://doi.org/10.1016/j.cej.2019.02.198>
- [67.] Landauer R (1978) Electrical conductivity in inhomogeneous media. In: AIP conference proceedings. AIP, pp 2–45
- [68.] McPherson R (1984) A model for the thermal conductivity of plasma-sprayed ceramic coatings. *Thin Solid Films* 112:89–95. [https://doi.org/10.1016/0040-6090\(84\)90506-6](https://doi.org/10.1016/0040-6090(84)90506-6)
- [69.] Schulz B (1981) Thermal conductivity of porous and highly porous materials. *High Temp High Press* 13:649–660
- [70.] Cernuschi F, Bianchi P, Leoni M, Scardi P (1999) Thermal diffusivity/microstructure relationship in Y-PSZ thermal barrier coatings. *J Therm Spray Technol* 8:102–109. <https://doi.org/10.1361/105996399770350629>
- [71.] Scardi P, Leoni M, Cernuschi F, Figari A (2001) Microstructure and heat transfer phenomena in ceramic thermal barrier coatings. *J Am Ceram Soc* 84:827–835. <https://doi.org/10.1111/j.1151-2916.2001.tb00748.x>
- [72.] Bianchi P, Cernuschi F, Lorenzoni L, et al (2002) Thermophysical and microstructural characterization of modified

- thick yttria stabilised zirconia thermal barrier coatings. In: Lecomte-Beckers J, Carton M, Schubert F, Ennis PJ (eds) *Materials for advanced power engineering 2002*. Schriften des Forschungszentrum Jülich, pp 449–463
- [73.] Maxwell JC (1873) *A treatise on electricity and magnetism*, vol I. Macmillan and Co. Publishers, London
- [74.] Bruggeman DAG (1937) Berechnung verschiedener physikalischer Konstanten von heterogenen Substanzen. III. Die elastischen Konstanten der quasiisotropen Mischkörper aus isotropen Substanzen. *Ann Phys* 421:160–178. <https://doi.org/10.1002/andp.19374210205>
- [75.] Schulz B (1974) Die Abhängigkeit der Feideigenschaften zweiphasiger Werkstoffe von ihrem Gefügeaufbau. Theoretische Überlegungen und experimentelle Prüfung am Beispiel der Wärmeleitfähigkeit von Cermets. Report KfK, FRG
- [76.] Meredith RE, Tobias CW (1962) *Conduction in heterogeneous systems*. In: *Advances in electrochemistry and electrochemical engineering*. New York
- [77.] Kosonowski A (2019) Bruggeman model visualization for porous materials. 1. <https://doi.org/10.17632/R639F4G276.1>

Publisher's Note Springer Nature remains neutral with regard to jurisdictional claims in published maps and institutional affiliations.